3D seismic image processing for unconformities

Xinming Wu & Dave Hale
Center for Wave Phenomena, Colorado School of Mines, Golden, CO 80401, USA

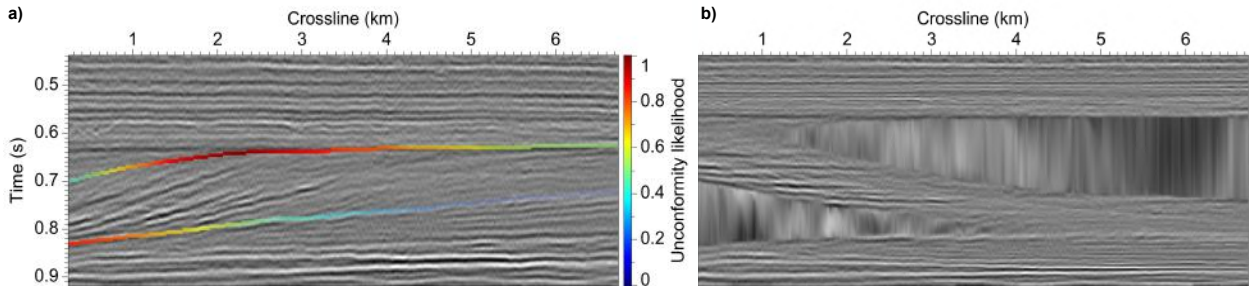

Figure 1. Unconformity likelihood (a) computed from a seismic image highlights unconformities, and can be used as constraints to more accurately estimate seismic normal vectors and better flatten (b) the seismic image.

ABSTRACT
We propose a 3D seismic unconformity attribute to detect complete unconformities, highlighting both their termination areas and correlative conformities. These detected unconformities are further used as constraints to more accurately estimate seismic normal vectors at unconformities. Then, using seismic normal vectors and detected unconformities as constraints, we can better flatten seismic images containing unconformities.

Key words: unconformity seismic normal vectors flattening

1 INTRODUCTION

An unconformity is a non-depositional or erosional surface separating older strata below from younger strata above, and thus represents a significant gap in geologic time (Vail et al., 1977). In seismic images, an unconformity can be first identified by seismic reflector terminations (i.e., *truncation, toplap, onlap or downlap*) and then be traced to its corresponding correlative conformity.

Unconformity detection is a significant aspect of seismic stratigraphic interpretation, because unconformities represent discontinuities in otherwise continuous depositions and hence serve as boundaries when interpreting *seismic sequences* that represent successively deposited layers.

Moreover, unconformities pose challenges for other automatic techniques used in seismic interpretation. First, it is difficult to accurately estimate normal vectors or slopes of seismic reflectors at an unconformity with multiply-oriented structures due to seismic reflector terminations. Second, automatic seismic flattening methods cannot correctly flatten reflectors at unconformities with geologic time gaps. To address these challenges, we first detect unconformities and then use them as constraints for seismic normal vector estimation and image flattening.

1.1 Unconformity detection

Seismic coherence (Bahorich and Farmer, 1995), which highlights reflector discontinuities, is used as a seismic attribute to detect faults and termination areas of unconformities. However, this coherence attribute is better suited for detecting faults than unconformities, because reflector discontinuities across a fault are usually more apparent than discontinuities across an unconformity. Hoek et al. (2010) propose a better unconformity attribute that measures the degree of seismic reflector convergence (or divergence), and thereby highlights the termination areas of an unconformity. Both of these methods process a seismic image locally (Ringdal, 2012) to

compute unconformity attributes that can highlight an unconformity within its termination area, but cannot detect its correlative conformity.

Ringdal (2012) proposes a global method that first extracts a 2D flow field that is everywhere tangent to reflectors in a 2D seismic image. Then the flow field is used to compute an unconformity probability image by repeating the following processing for each sample: four seeds are first placed at the four neighbors of the sample in the 2D flow field; the four seeds then move along the flow field to produce trajectories; the separation rate of the trajectories is finally calculated and used as unconformity probability for that sample. The advantage of this method is that it can use long trajectories to detect the correlative conformity of an unconformity. The disadvantage is that, to detect such a correlative conformity, the trajectories are required to start from the parallel area (correlative conformity) and end in the non-parallel area (termination). For 3D seismic images, this method processes inline and crossline slices separately throughout the volume to compute an unconformity probability volume.

1.2 Seismic normal vector estimation

Orientation vector fields, such as vectors normal to or slopes of seismic reflectors, are useful for seismic interpretation. For example, estimated orientation information is used to control slope-based (Fomel, 2002) and structure-oriented (Fehmers and Höcker, 2003; Hale, 2009) filters so that they smooth along reflectors to enhance their coherencies. Seismic normal vectors or slopes are also used to flatten (Lomask et al., 2006; Parks, 2010) or unfold (Luo and Hale, 2013) seismic images, or to generate horizon volumes (Wu and Hale, 2014).

Structure tensors (van Vliet and Verbeek, 1995; Fehmers and Höcker, 2003) or plane-wave destruction filter (Fomel, 2002) have been proposed to estimate seismic normal vectors or slopes. These methods can accurately estimate orientation vectors for structures with only one locally dominant orientation. This means that they can correctly estimate the normal vectors (or slopes) of the reflectors in conformable areas of a seismic image, but for an angular unconformity where two different structures meet, these methods yield smoothed vectors that represent averages of orientations across the unconformity.

1.3 Seismic image flattening

Seismic image flattening (Lomask et al., 2006; Parks, 2010; Wu and Hale, 2014) or unfolding (Luo and Hale, 2013) methods are applied to a seismic image to obtain a flattened image in which all seismic reflectors are horizontal. From such a flattened seismic image, all seismic horizons can be identified by simply slicing horizontally.

Extracting horizons terminated by faults or unconformities is generally difficult for these methods. Luo and Hale (2013) extract horizons across faults by first unfaulting a seismic image; Wu and Hale (2014) do the same by placing control points on opposite sides of faults. However, none of these methods correctly flattens a seismic image with unconformities, which should produce gaps in the flattened image (e.g., Figure 1b).

1.4 This paper

In this paper, we first propose a method to automatically detect an unconformity, complete with its termination area and correlative conformity, as shown in Figure 1a. We then describe how to more accurately estimate seismic normal vectors at unconformities by using the detected unconformities as constraints. Finally, we discuss how to better flatten (Figure 1b) seismic images containing unconformities by using these estimated seismic normal vectors and again using constraints derived from detected unconformities.

2 UNCONFORMITY DETECTION

In manual 3D seismic stratigraphic interpretations, an unconformity is first recognized as a border at which seismic reflectors terminate (i.e., truncation, toplap, onlap or downlap), and then is traced to its correlative conformities where reflectors are parallel. Therefore, to obtain a complete unconformity, an automatic method should be able to detect both the termination areas (green ellipse in Figure 2a) and correlative conformities (dashed blue ellipse in Figure 2a) within the unconformity.

We propose an unconformity attribute that measures differences between two seismic normal vector fields computed from two structure-tensor fields, one is computed using a vertically causal smoothing filter, and the other using a vertically anti-causal smoothing filter. This attribute can highlight both the termination areas and correlative conformities of an unconformity.

2.1 Structure tensor

The structure tensor (van Vliet and Verbeek, 1995; Fehmers and Höcker, 2003) can be used to estimate seismic normal vectors that are perpendicular to seismic reflectors. For a 2D image, the structure tensor $\mathbf{T}$ for each sample is a 2×2 symmetric positive-semidefinite matrix constructed as the smoothed outer product of image gradients:

$$\mathbf{T} = \langle \mathbf{g}\mathbf{g}^\top \rangle_{h,v} = \begin{bmatrix} \langle g_1 g_1 \rangle_{h,v} & \langle g_1 g_2 \rangle_{h,v} \\ \langle g_1 g_2 \rangle_{h,v} & \langle g_2 g_2 \rangle_{h,v} \end{bmatrix}, \qquad (1)$$

where $\mathbf{g} = [g_1 \ g_2]^\top$ represents the image gradient vector computed for each image sample; $\langle \cdot \rangle_{h,v}$ represents

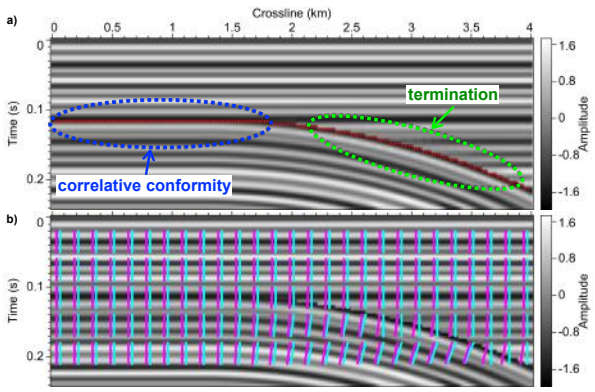

Figure 2. A 2D synthetic seismic image (a) with an unconformity (red curve) that is manually extended from its termination area to its correlative unconformity. The estimated seismic normal vectors (magenta segments in (b)) are smoothed within the termination area, and therefore are incorrect, compared to the true seismic normal vectors (cyan segments in (b)) that are discontinuous within that area.

smoothing in both horizontal (subscript h) and vertical (subscript v) directions. These horizontal and vertical smoothing filters are commonly implemented with Gaussian filters with corresponding half-widths σ_h and σ_v.

As shown by Fehmers and Höcker (2003), the seismic normal vector for each image sample can be estimated from the eigen-decomposition of the structure tensor $\mathbf{T}$:

$$\mathbf{T} = \lambda_u \mathbf{u}\mathbf{u}^\top + \lambda_v \mathbf{v}\mathbf{v}^\top, \tag{2}$$

where $\mathbf{u}$ and $\mathbf{v}$ are unit eigenvectors corresponding to eigenvalues λ_u and λ_v of $\mathbf{T}$.

We choose $\lambda_u \geq \lambda_v$, so that the eigenvector $\mathbf{u}$, which corresponds to the largest eigenvalue λ_u, indicates the direction of highest change in image amplitude, and therefore is perpendicular to locally linear features in an image, while the orthogonal eigenvector $\mathbf{v}$ indicates the direction that is parallel to such features. In other words, the eigenvector $\mathbf{u}$ is the seismic normal vector that is perpendicular to seismic reflectors in a seismic image, and the eigenvector $\mathbf{v}$ is parallel to the reflectors.

2.2 Smoothing

The structure tensor $\mathbf{T}$ given in equation 1 can be used to accurately estimate the local orientation of structures in an image where there is only one locally dominant orientation present. However, for multiply-oriented structures such as an unconformity where seismic reflectors terminate (dashed green ellipse in Figure 2a), this structure tensor provides a local average of the orientations of structures. The seismic normal vectors (magenta segments in Figure 2b) estimated from $\mathbf{T}$ are smoothed near the termination area, whereas the true normal vectors (cyan segments in Figure 2b) are discontinuous across the unconformity.

At an unconformity where seismic reflectors terminate (dashed green ellipse in Figure 2a), structures of reflectors above the unconformity are different from those of reflectors below. Therefore, if we compute structure tensors using vertically causal smoothing filters, which average structures from above, we will obtain normal vectors at the unconformity that are different from those obtained using vertical anti-causal filters, which average structures from below.

With a vertically causal filter, the structure tensor computed for each sample represents structures averaged using only samples above. We define such a structure tensor as

$$\mathbf{T}_c = \begin{bmatrix} \langle g_1 g_1 \rangle_{h,vc} & \langle g_1 g_2 \rangle_{h,vc} \\ \langle g_1 g_2 \rangle_{h,vc} & \langle g_2 g_2 \rangle_{h,vc} \end{bmatrix}, \tag{3}$$

where $\langle \cdot \rangle_{h,vc}$ represents horizontal Gaussian (subscript h) and vertically causal (subscript vc) smoothing filters.

With a vertically anti-causal filter, the structure tensor computed for each sample represents structures averaged using only samples below. We define such a structure tensor as

$$\mathbf{T}_a = \begin{bmatrix} \langle g_1 g_1 \rangle_{h,va} & \langle g_1 g_2 \rangle_{h,va} \\ \langle g_1 g_2 \rangle_{h,va} & \langle g_2 g_2 \rangle_{h,va} \end{bmatrix}, \tag{4}$$

where the subscript va denotes a vertically anti-causal smoothing filter.

2.2.1 Vertical smoothing

To compute two structure-tensor fields that differ significantly at an unconformity, the causal smoothing filter that averages from above should smooth along the direction perpendicular to the structures above the unconformity, while the anti-causal filter should smooth along the direction perpendicular to the structures below the unconformity. Here, we simply use vertically causal and anti-causal filters because unconformities are usually tend to be horizontal in seismic images. We implement these two filters with one-sided exponential smoothing filters, which are efficient and trivial to implement.

A one-sided causal exponential filter for input and output sequences `x[i]` and `y[i]` with lengths `n` can be implemented in C++ (or Java) as follows:

```
float b = 1.0f-a;
float yi = y[0] = x[0];
for (int i=1; i<n; ++i)
  y[i] = yi = a*yi+b*x[i];
```

Similarly, a one-sided anti-causal exponential filter can be implemented as follows:

```
float b = 1.0f-a;
float yi = y[n-1] = x[n-1];
for (int i=n-2; i>=0; --i)
  y[i] = yi = a*yi+b*x[i];
```

The parameter `a` in these two one-sided exponential fil-

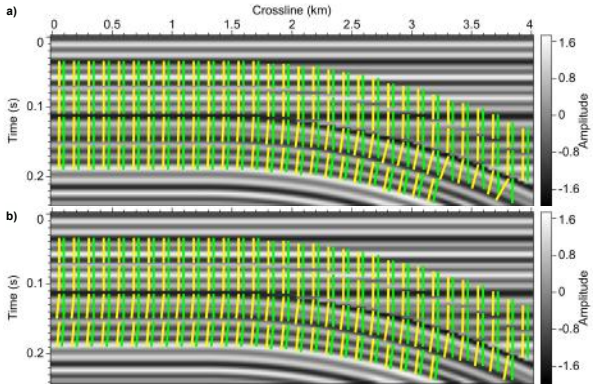

Figure 3. Two different seismic normal vector fields estimated using structure tensors computed with vertically causal (yellow segments) and anti-causal (green segments) smoothing filters. In (a), the vector fields differ only within the termination area of the unconformity; in (b), these vector differences are extended to the correlative conformity.

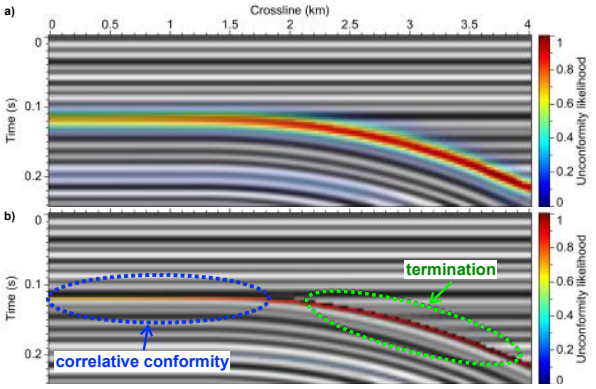

Figure 4. Unconformity likelihoods, an attribute that evaluates differences between two estimated seismic normal vector fields (yellow and green segments in Figure 3b), before (a) and after (b) thinning highlight both the termination area and correlative conformity of the unconformity.

ters controls the extent of smoothing.

From structure-tensor fields $\mathbf{T}_c$ and $\mathbf{T}_a$ computed for the same seismic image using vertically causal and anti-causal smoothing filters, respectively, we estimate two seismic normal vector fields $\mathbf{u}_c$ and $\mathbf{u}_a$. As shown in Figure 3a, the two seismic normal vector fields $\mathbf{u}_c$ (green segments in Figure 3a) and $\mathbf{u}_a$ (yellow segments in Figure 3a) are identical in conformable areas with parallel seismic reflectors, because orientation of structures locally averaged from above (used to compute $\mathbf{T}_c$) are identical to orientation of structures averaged from below (used to compute $\mathbf{T}_a$). However, at the termination area of an unconformity, the two vector fields are different, because the structure tensors $\mathbf{T}_c$ computed with structures locally averaged from above, should be different from $\mathbf{T}_a$ computed with structures locally averaged from below.

Therefore, as shown in Figure 3a, the difference between estimated normal vector fields $\mathbf{u}_c$ and $\mathbf{u}_a$ provides a good indication of the termination area of an unconformity. However, a complete unconformity, that is, a curve (in 2D) or surface (in 3D) with geologic time gaps, extends from its termination area its correlative conformity with. Thus we should extend normal vector differences from the termination area, where these differences originate, to the correlative conformity.

2.2.2 Structure-oriented smoothing

To detect a correlative conformity, we extend vector differences (between $\mathbf{u}_c$ and $\mathbf{u}_a$) at an unconformity from its termination area to its correlative conformity, by replacing the horizontal Gaussian smoothing filter in equations 3 and 4 with a structure-oriented smoothing filter (Hale, 2009) when computing structure tensors.

Then, the structure tensors $\mathbf{T}_{s,c}$ and $\mathbf{T}_{s,a}$, computed with a laterally structure-oriented filter and vertically causal and anti-causal filters, are defined by

$$\mathbf{T}_{s,c} = \begin{bmatrix} \langle g_1 g_1 \rangle_{s,vc} & \langle g_1 g_2 \rangle_{s,vc} \\ \langle g_1 g_2 \rangle_{s,vc} & \langle g_2 g_2 \rangle_{s,vc} \end{bmatrix}, \tag{5}$$

and

$$\mathbf{T}_{s,a} = \begin{bmatrix} \langle g_1 g_1 \rangle_{s,va} & \langle g_1 g_2 \rangle_{s,va} \\ \langle g_1 g_2 \rangle_{s,va} & \langle g_2 g_2 \rangle_{s,va} \end{bmatrix}, \tag{6}$$

where the subscript s represents a structure-oriented filter that smoothes along reflectors in a seismic image. Note that the structure-oriented smoothing is generally more expensive than the vertically causal and anti-causal smoothing. We therefore first apply the structure-oriented smoothing filter to each element of $\mathbf{g}\mathbf{g}^\top$ to obtain $\mathbf{T}_s = \langle \mathbf{g}\mathbf{g}^\top \rangle_s$, which then is smoothed separately by vertically causal and anti-causal filters to obtain $\mathbf{T}_{s,c}$ and $\mathbf{T}_{s,a}$, respectively. By doing this, we apply the relatively expensive structure-oriented smoothing only once. However, if we first apply the vertically causal and anti-causal smoothing to compute two differently smoothed outer products $\langle \mathbf{g}\mathbf{g} \rangle_c$ and $\langle \mathbf{g}\mathbf{g}^\top \rangle_a$, we then need to apply the structure-oriented smoothing twice to obtain two structure-tensor fields $\mathbf{T}_{s,c}$ and $\mathbf{T}_{s,a}$.

As discussed by Hale (2009, 2011), to obtain a smoothed output image $q(\mathbf{x})$ from an input $p(\mathbf{x})$, the structure-oriented smoothing method solves a finite-difference approximation to the following partial differential equation:

$$q(\mathbf{x}) - \frac{\sigma^2}{2} \boldsymbol{\nabla} \cdot \mathbf{D}(\mathbf{x}) \cdot \boldsymbol{\nabla}\, q(\mathbf{x}) = p(\mathbf{x}), \tag{7}$$

where $\mathbf{D}(\mathbf{x})$ is a diffusion-tensor field that shares the eigenvectors of the structure tensor computed from an image, and therefore orients the smoothing along image structures. Similar to the half-width σ in a Gaussian smoothing filter, the parameter σ controls the extent of

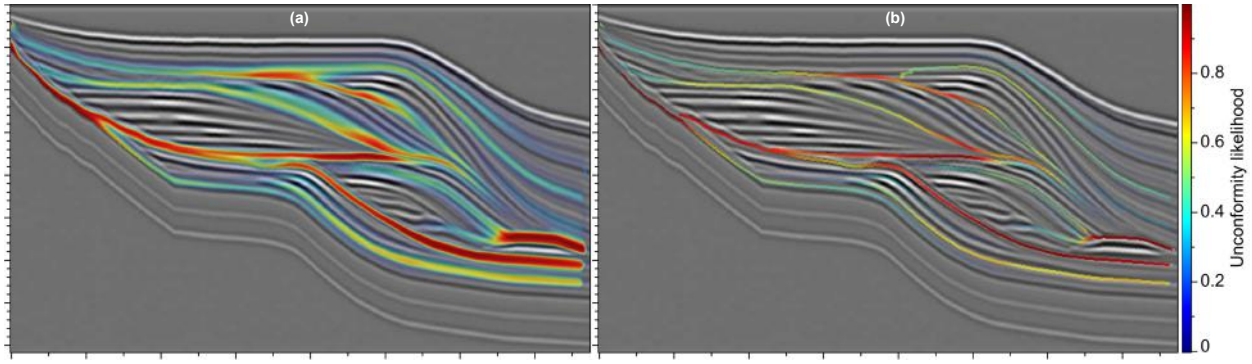

Figure 5. Applying our method to the synthetic image cut from Hoek et al. (2010), we obtain unconformity likelihoods before (a) and after (b) thinning.

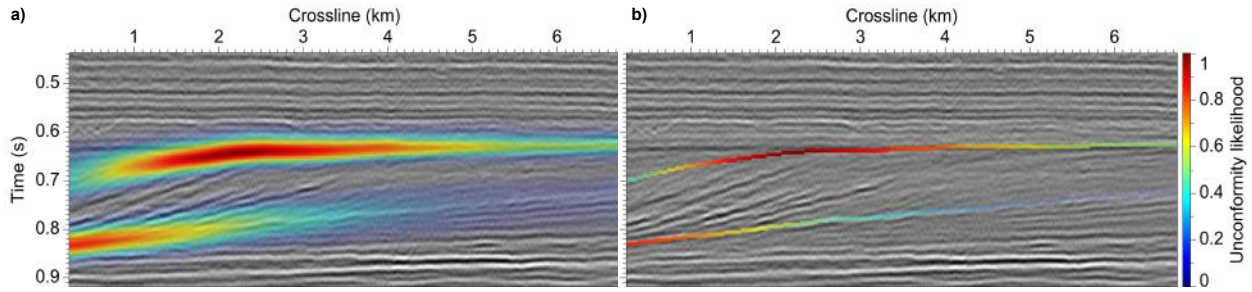

Figure 6. Unconformity likelihoods before (a) and after (b) thinning.

smoothing.

In 2D, we use the eigenvectors $\mathbf{u}(\mathbf{x})$ and $\mathbf{v}(\mathbf{x})$, estimated using the structure tensors shown in equation 1, to construct our diffusion-tensor field

$$\mathbf{D}(\mathbf{x}) = \lambda_u(\mathbf{x})\mathbf{u}(\mathbf{x})\mathbf{u}^\top(\mathbf{x}) + \lambda_v(\mathbf{x})\mathbf{v}(\mathbf{x})\mathbf{v}^\top(\mathbf{x}). \qquad (8)$$

Then, because eigenvectors $\mathbf{u}(\mathbf{x})$ and $\mathbf{v}(\mathbf{x})$ are perpendicular and parallel to seismic reflectors, respectively, we can control the structure-orient filter to smooth along reflectors by setting the corresponding eigenvalues $\lambda_u(\mathbf{x}) = 0$ and $\lambda_v(\mathbf{x}) = 1$ for all tensors in $\mathbf{D}(\mathbf{x})$.

As indicated by the seismic normal vectors shown in Figure 2b, normal vectors (magenta segments) estimated using the structure tensors computed in equation 1 are inaccurate at unconformities. However, they are accurate in conformable areas, including the area near correlative conformity of the unconformity. Thus the structure tensors in equation 1 are adequate for constructing diffusion-tensors $\mathbf{D}(\mathbf{x})$ for structure-oriented smoothing along seismic reflectors, including those near the correlative conformity of an unconformity. By applying such a structure-oriented filter to the elements of the structure tensors $\mathbf{T}_{s,c}$ and $\mathbf{T}_{s,a}$, we extend structural differences, originating within the termination area of an unconformity, to the corresponding correlative conformity.

As shown in Figure 3, using structure tensors $\mathbf{T}_c$ and $\mathbf{T}_a$ computed with a horizontal Gaussian filter and vertically causal and anti-causal filters, the estimated seismic normal vectors $\mathbf{u}_c$ (green segments in Figure 3a) and $\mathbf{u}_a$ (yellow segments in Figure 3a) differ only within the termination area of the unconformity. Using structure tensors $\mathbf{T}_{s,c}$ and $\mathbf{T}_{s,a}$ computed with a structure-oriented smoothing filter instead of a horizontal Gaussian filter, the differences between the estimated seismic normal vectors $\mathbf{u}_{s,c}$ (green segments in Figure 3b) and $\mathbf{u}_{s,a}$ (yellow segments in Figure 3b) are extended from the termination area to the correlative area.

In summary, by first applying a structure-oriented filter to each structure-tensor element of $\mathbf{g}\mathbf{g}^\top$, we extend any structure differences, which originate within the termination area of an unconformity, to its correlative conformity. Then, applying vertically causal and anti-causal filters for each structure-tensor element, we compute two different structure-tensor fields $\mathbf{T}_{s,c}$ and $\mathbf{T}_{s,a}$ with seismic normal vector fields $\mathbf{u}_{s,c}$ and $\mathbf{u}_{s,a}$ that differ within both the termination area and correlative conformity of an unconformity. Finally, the differences between the two estimated vector fields $\mathbf{u}_{s,c}$ and $\mathbf{u}_{s,a}$ can be used as an unconformity attribute that highlights the complete unconformity.

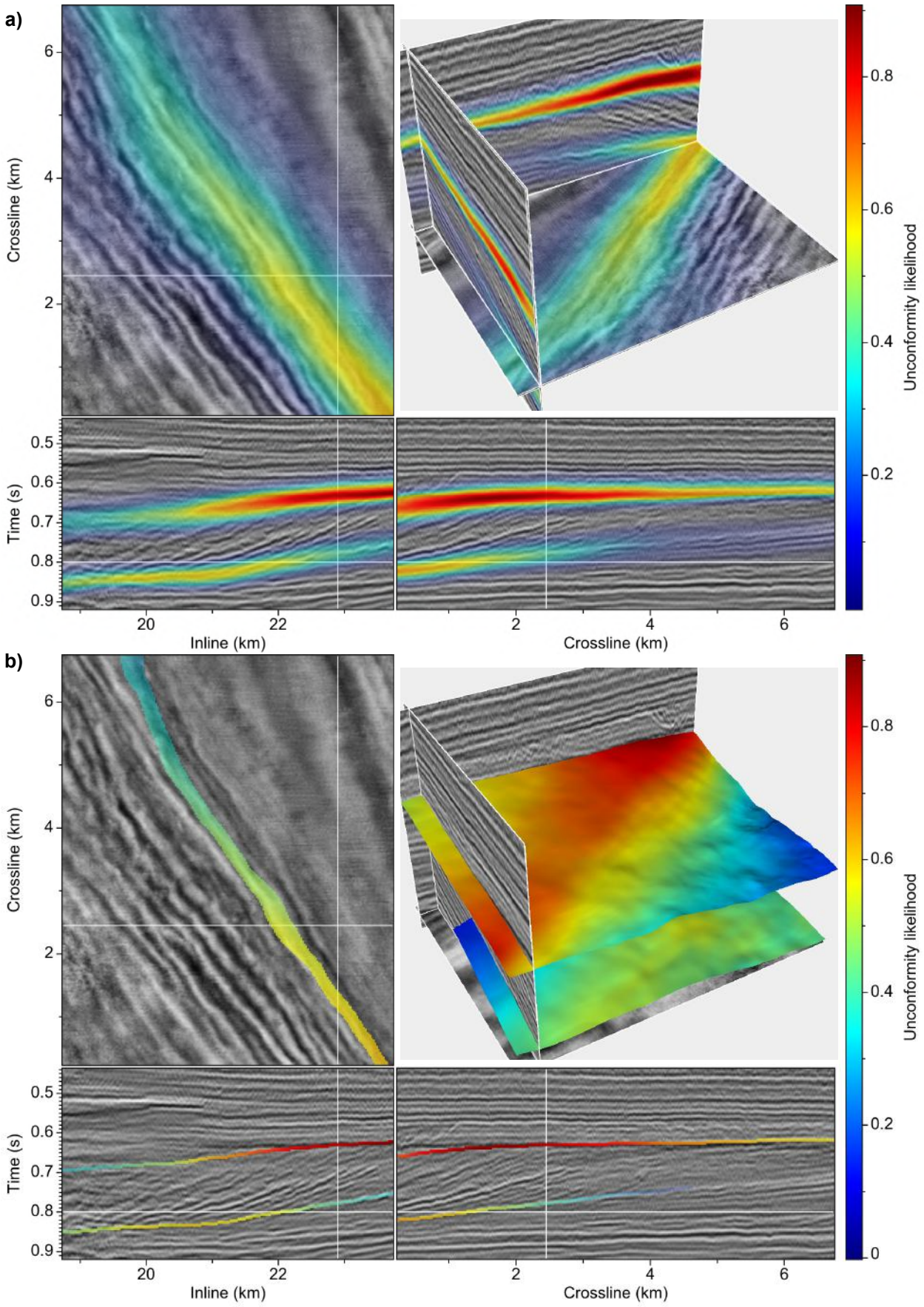

Figure 7. Unconformity likelihoods before (a) and after (b) thinning. Thinned unconformity likelihoods form unconformity surfaces (b).

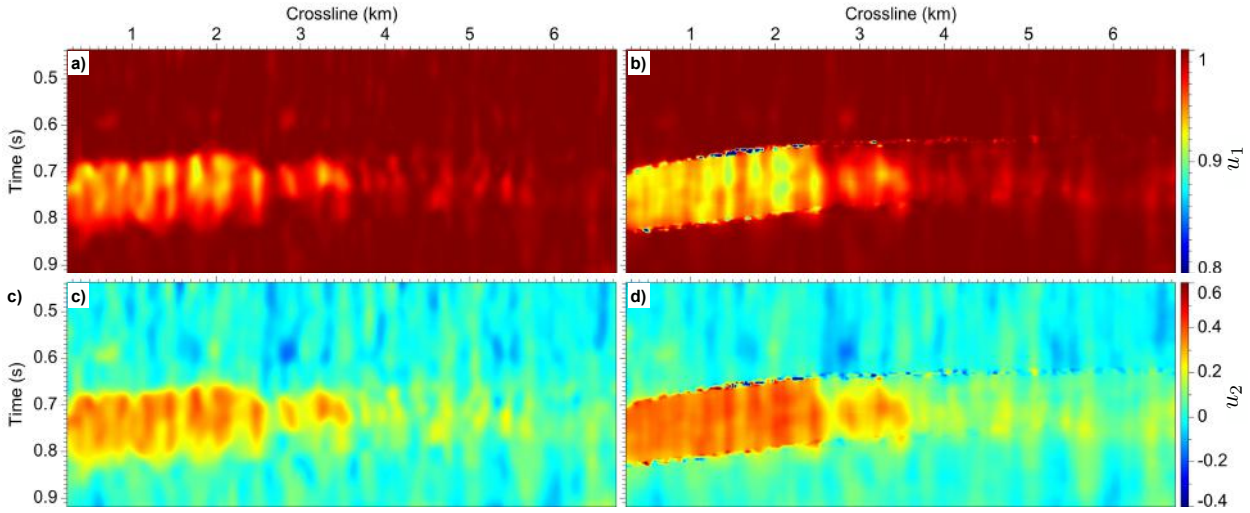

Figure 8. Vertical (u_1) and horizontal (u_2) components of seismic normal vectors estimated using structure tensors computed with (b, d) and without (a, c) unconformity constraints.

2.3 Unconformity likelihood

As shown in Figure 3b, the vectors $\mathbf{u}_{s,c}$ (green segments) and $\mathbf{u}_{s,a}$ (yellow segments) are identical everywhere except at the unconformity, including its termination area and correlative conformity. Therefore, we define an *unconformity likelihood* attribute g, that evaluates the differences between $\mathbf{u}_{s,c}$ and $\mathbf{u}_{s,a}$, to highlight unconformities:

$$g \equiv 1 - (\mathbf{u}_{s,c} \cdot \mathbf{u}_{s,a})^p. \tag{9}$$

A large power p ($p \gg 1$) increases the contrast between samples with low and high unconformity likelihoods. For the example shown in Figure 4a, the unconformity likelihoods are computed with $p = 200$.

Using a process similar to that used by Hale (2012) for extracting ridges of fault likelihoods, we extract ridges of unconformity likelihood by simply scanning each vertical column of the unconformity likelihood image (Figure 4a), preserving only local maxima, and setting unconformity likelihoods elsewhere to zero. Figure 4b shows that ridges of unconformity likelihood coincide with the unconformity that appears in the synthetic seismic image.

Figure 5 shows a more complicated 2D synthetic image used by Hoek et al. (2010). The geometric attributes they compute highlight only the termination areas of unconformities apparent in this synthetic image. In comparison, unconformity likelihoods before (Figure 5a) and after (Figure 5b) thinning, computed using our method, highlight the complete unconformities, including their termination areas as well as correlative conformities.

Figure 6 shows an example of a real 2D seismic image, in which generated unconformity likelihoods before (Figure 6a) and after (Figure 6b) thinning correctly highlight two unconformities apparent in the seismic image.

For a 3D seismic image, following the same process as above, we compute an unconformity-likelihood volume as shown in Figure 7, which correctly highlights two apparent unconformities. In the time slices of unconformity likelihoods before and after thinning, we observe that samples in the lower-left and upper-right areas, separated by high unconformity likelihoods, suggest different seismic facies. This indicates that they belong to two different depositional sequences that have different geologic times.

From ridges of unconformity likelihoods (Figure 7b), we connect adjacent samples with high unconformity likelihoods to form unconformity surfaces as shown in upper-right panel of Figure 7b.

3 APPLICATIONS

We first use unconformity likelihoods as constraints to more accurately estimate seismic normal vectors at unconformities. Then, using more accurate normal vectors and unconformity likelihoods as constraints in our seismic image flattening method, we are able to better flatten an image containing unconformitities.

3.1 Estimation of seismic normal vectors at unconformities

Using structure tensors computed with horizontal and vertical Gaussian filters as shown in equation 1, we find smoothed seismic normal vectors (magenta segments in Figure 2b) in the termination area, because discontinuous structures across the unconformity are smoothed

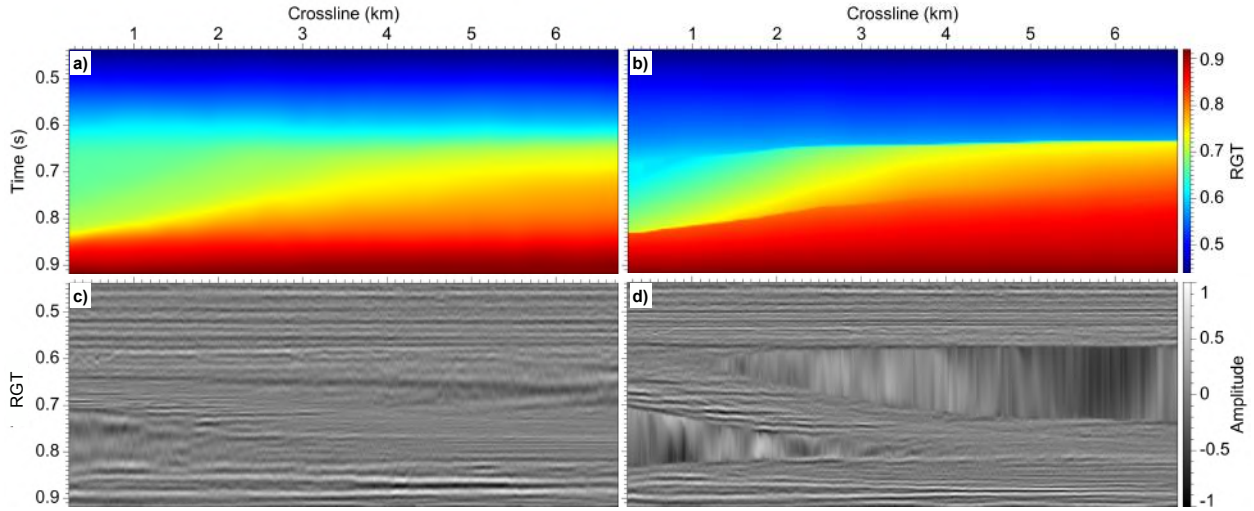

Figure 9. RGT (a) and flattened (c) images generated with inaccurate seismic normal vectors (Figures 8a and 8c) and without unconformity constraints. Improved RGT (b) and flattened (d) images with more accurate seismic normal vectors (Figures 8b and 8d) and constraints from unconformity likelihoods (Figure 6).

by symmetric Gaussian filters. Therefore, to obtain correct normal vectors (cyan segments in Figure 2b) that are discontinuous in the termination area, we must use more appropriate filters to compute structure tensors.

To preserve structure discontinuities, we compute the structure tensors using horizontal and vertical filters that do not smooth across unconformities:

$$\mathbf{T} = \begin{bmatrix} \langle g_1 g_1 \rangle_{sh,sv} & \langle g_1 g_2 \rangle_{sh,sv} \\ \langle g_1 g_2 \rangle_{sh,sv} & \langle g_2 g_2 \rangle_{sh,sv} \end{bmatrix}, \tag{10}$$

where the $\langle \cdot \rangle_{sh,sv}$ represent horizontal (subscript sh) and vertical (subscript sv) filters that vary spatially, and for which the extent of smoothing is controlled by the thinned unconformity likelihoods.

The horizontal and vertical filters are similar to the edge-preserving smoothing filter discussed in Hale (2011):

$$q(\mathbf{x}) - \frac{\sigma^2}{2} \boldsymbol{\nabla} \cdot c^2(\mathbf{x}) \cdot \boldsymbol{\nabla}\, q(\mathbf{x}) = p(\mathbf{x}). \tag{11}$$

We compute $c(\mathbf{x}) = 1 - g_t(\mathbf{x})$ to prevent this filter from smoothing across unconformities. $g_t(\mathbf{x})$ is a thinned unconformity likelihood image as shown in Figure 6b, which has large values (close to 1) only at unconformities and zeros elsewhere.

Figure 8 shows seismic normal vectors estimated for the image with two unconformities shown in Figure 6. Both the vertical (Figure 8a) and horizontal (Figure 8c) components of seismic normal vectors, estimated from structure tensors computed as in equation 1, are smooth at the unconformities; those estimated from structure tensors computed as in equation 10 preserve discontinuities at unconformities (Figures 8b and 8d).

3.2 Seismic image flattening at unconformities

Seismic normal vectors or dips can be used to flatten (Lomask et al., 2006; Parks, 2010) or unfold (Luo and Hale, 2013) a seismic image to generate a horizon volume (Wu and Hale, 2014), that allows for the extraction of all seismic horizons in the image. Faults and unconformities, which represent discontinuities of reflectors in a seismic image, present challenges for these methods. Luo and Hale (2013) and Wu and Hale (2014) have extended their methods to handle faults by first unfaulting the seismic image or by placing control points on opposite sides of a fault. However, neither of these methods correctly handles seismic images with unconformities, because estimated seismic normal vectors or dips are inaccurate at unconformities, and because unconformities are not automatically detected and then used as constraints in these methods.

In this paper we have proposed methods to automatically detect unconformities and more accurately estimate seismic normal vectors at unconformities. Therefore, we can easily extend the flattening method described in Wu and Hale (2014), to better flatten a seismic image at unconformities, by using seismic normal vectors estimated from structure tensors computed with equation 10, and by incorporating constraints derived from unconformity likelihoods into the flattening method. We incorporate unconformity constraints in our flattening method by weighting the equations for flattening using unconformity likelihoods, and then using the unconformity likelihoods to construct preconditioner in the conjugate gradient method used to solve those equations.

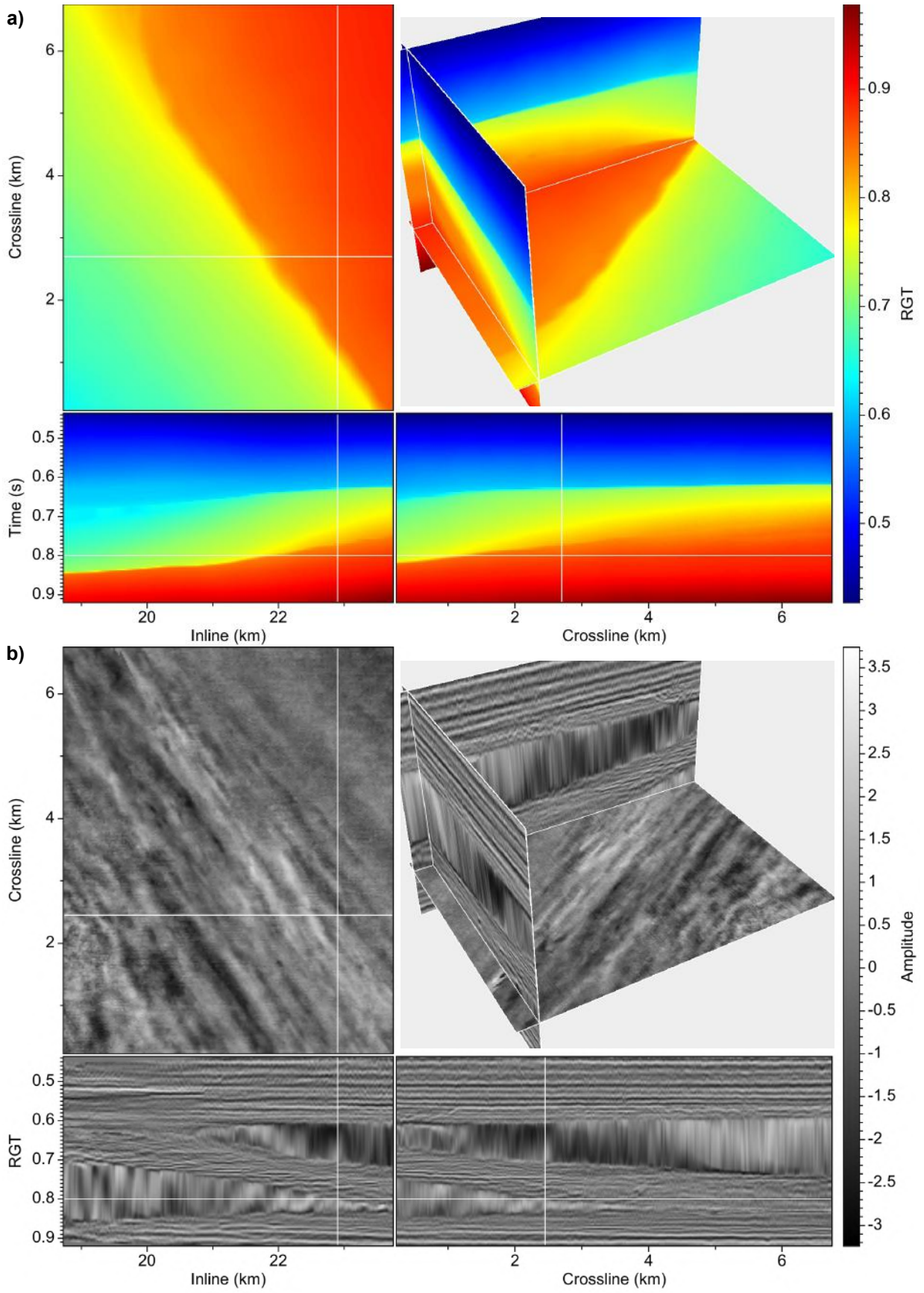

Figure 10. Generated RGT volume (a) and flattened (b) 3D seismic image. Discontinuities in the RGT volume correspond to vertical gaps in the flattened image at unconformities.

3.2.1 Weighting

To generate a horizon volume or to flatten a seismic image, we first solve for vertical shifts $s(x,y,z)$ as discussed in Wu and Hale (2014):

$$\begin{bmatrix} w(-\frac{\partial s}{\partial x} - p\frac{\partial s}{\partial z}) \\ w(-\frac{\partial s}{\partial y} - p\frac{\partial s}{\partial z}) \\ \epsilon\frac{\partial s}{\partial z} \end{bmatrix} \approx \begin{bmatrix} wp \\ wq \\ 0 \end{bmatrix}, \tag{12}$$

where $p(x,y,z)$ and $q(x,y,z)$ are inline and crossline reflector slopes computed from seismic normal vectors; $w(x,y,z)$ represent weights for the equations; and the third equation $\epsilon\frac{\partial s}{\partial z} \approx 0$, scaled by a small constant ϵ, is used to reduce rapid vertical variations in the shifts.

For a seismic image with unconformities, we incorporate constraints derived from unconformity likelihoods into the equations 12 by setting $w(x,y,z) = 1 - g_t(x,y,z)$ and we use a spatially variant $\epsilon(x,y,z)$ instead of a constant value:

$$\epsilon(x,y,z) = \epsilon_0(1 - g_t(x,y,z)), \tag{13}$$

where ϵ_0 is a small constant number (we use $\epsilon_0 = 0.01$ for all examples in this paper), and $g_t(x,y,z)$ denotes the thinned unconformity likelihoods, such as those shown in Figure 7b.

This spatially variant $\epsilon(x,y,z)$, with smaller values (nearly 0) at unconformities, helps to generate more reasonable shifts with gradual variations everywhere except at unconformities.

3.2.2 Preconditioner

As discussed in Wu and Hale (2014), to obtain the shifts $s(x,y,z)$ in equation 12 for a 3D seismic image with N samples, we solve its corresponding least-squares problem expressed in a matrix form:

$$(\mathbf{WG})^\top\mathbf{WGs} = (\mathbf{WG})^\top\mathbf{Wv}, \tag{14}$$

where $\mathbf{s}$ is an $N\times 1$ vector containing the unknown shifts $s(x,y,z)$, $\mathbf{G}$ is a $3N \times N$ sparse matrix representing finite-difference approximations of partial derivatives, $\mathbf{W}$ is a $3N \times 3N$ diagonal matrix containing weights $w(x,y,z)$ and $\epsilon(x,y,z)$, and $\mathbf{v}$ is a $3N \times 1$ vector with $2N$ slopes p and q, and N zeros.

Because the matrix $(\mathbf{WG})^\top\mathbf{WG}$ is symmetric positive-semidefinite, we can solve the linear system of equation 14 using the preconditioned conjugate gradient method, with a preconditioner $\mathbf{M}^{-1}$ as in Wu and Hale (2014):

$$\mathbf{M^{-1}} = \mathbf{S}_x\mathbf{S}_y\mathbf{S}_z\mathbf{S}_z^\top\mathbf{S}_y^\top\mathbf{S}_x^\top, \tag{15}$$

where $\mathbf{S}_x$, $\mathbf{S}_y$ and $\mathbf{S}_z$ are filters that smooth in the x, y and z directions, respectively.

For a seismic image with unconformities, the filters $\mathbf{S}_x$, $\mathbf{S}_y$ and $\mathbf{S}_z$ are spatially variant filters designed as in equation 11, to preserve discontinuities in shifts $s(x,y,z)$ at unconformities.

3.2.3 Results

With the computed shifts $s(x,y,z)$, we first generate a relative geologic time (RGT) volume $\tau(x,y,z) = z + s(x,y,z)$ (Figures 9a and 10a). We then use the RGT volume to map a seismic image $f(x,y,z)$ (Figures 6 or 7) in the depth-space domain to a flattened image $\tilde{f}(x,y,\tau)$ (Figures 9b or 10b) in the RGT-space domain.

From the 2D example shown in Figure 9, the RGT (Figure 9a) and flattened (Figure 9c) images, generated with inaccurate seismic normal vectors (Figure 8a and 8c) and without unconformity constraints, are incorrect at unconformities, where we expect discontinuities in the RGT image and corresponding gaps in the flattened image. With more accurate seismic normal vectors (Figure 8b and 8d) and with constraints derived from unconformity likelihoods (Figure 6), we obtain an improved RGT image (Figure 9b) with discontinuities at unconformities. Using this RGT image, we obtain an improved flattened image (Figure 9c), in which seismic reflectors are horizontally flattened and unconformities appear as vertical gaps.

Figure 10 shows a 3D example with two unconformity surfaces, highlighted by unconformity likelihoods in Figure 7. We observe obvious discontinuities in RGT at unconformities in our generated RGT volume (Figure 10a). These RGT discontinuities result in vertical gaps in the corresponding flattened seismic image (Figure 10b). The time slice of an RGT image shows large RGT variations between samples in the lower-left and upper-right areas that are separated by an unconformity. This indicates that the sediments, represented by the samples in the two different areas, are deposited in two different sedimentary sequences occurring at different geologic times.

4 CONCLUSION

We have proposed a method to obtain an unconformity likelihood attribute from the differences between two seismic normal vector fields estimated from two structure-tensor fields, one is computed using a vertically causal smoothing filter, and the other using a vertically anti-causal filter. From a seismic image, we first compute smoothed outer products of image gradients by applying a structure-oriented smoothing filter to each element of these outer products. These smoothed outer products are then smoothed using vertically causal and anti-causal filters to compute two different structure-tensor fields, and their corresponding normal vector fields.

Using structure-oriented smoothing filters for the

outer products, we extend structure variations from a termination area to the corresponding correlative conformity. In doing this, we assume that the correlative conformity is not dislocated by faults. If faults appear in the seismic image, we could perform unfaulting (Luo and Hale, 2013) before attempting to detect unconformities.

We use separate vertically causal and anti-causal filters to obtain structure tensors that differ at unconformities. Unconformity likelihoods might be further improved by instead using causal and anti-causal filters that smooth in directions orthogonal to unconformities.

As examples of applications, we have shown how to estimate more accurate seismic normal vectors and better flatten seismic reflectors at unconformities by using unconformity likelihoods as constraints.

ACKNOWLEDGMENTS

This research is supported by the sponsor companies of the Consortium Project on Seismic Inverse Methods for Complex Structures. All of the real seismic images shown in this paper were provided by the US Department of Energy and by dGB Earth Sciences. The 2D synthetic seismic image used in the example shown in Figure 5 is that shown in Hoek et al. (2010).

REFERENCES

Bahorich, M., and S. Farmer, 1995, 3-D seismic discontinuity for faults and stratigraphic features: The coherence cube: The Leading Edge, **14**, 1053–1058.

Fomel, S., 2002, Applications of plane-wave destruction filters: Geophysics, **67**, 1946–1960.

Hale, D., 2009, Structure-oriented smoothing and semblance: CWP Report 635.

———, 2011, Structure-oriented bilateral filtering: 81st Annual International Meeting, SEG, Expanded Abstracts, 3596–3600.

———, 2012, Methods to compute fault images, extract fault surfaces, and estimate fault throws from 3D seismic images: Geophysics, **78**, O33–O43.

Hoek, T. V., S. Gesbert, and J. Pickens, 2010, Geometric attributes for seismic stratigraphic interpretation: The Leading Edge, **29**, 1056–1065.

Lomask, J., A. Guitton, S. Fomel, J. Claerbout, and A. A. Valenciano, 2006, Flattening without picking: Geophysics, **71**, 13–20.

Luo, S., and D. Hale, 2013, Unfaulting and unfolding 3D seismic images: Geophysics, **78**, O45–O56.

Fehmers, G. C., and C. Höcker, 2003, Fast structural interpretation with structure-oriented filtering: Geophysics, **68**, 1286–1293.

Parks, D., 2010, Seismic image flattening as a linear inverse problem: Master's thesis, Colorado School of Mines.

Ringdal, K., 2012, Flow-based segmentation of seismic data: Master's thesis, University of Bergen.

Vail, P. R., R. G. Todd, and J. B. Sangree, 1977, Seismic stratigraphy and global changes of sea level: Part 5. chronostratigraphic significance of seismic reflections: Section 2. application of seismic reflection configuration to stratigraphic interpretation: M 26: Seismic Stratigraphy–Applications to Hydrocarbon Exploration, AAPG Memoirs, 99–116.

van Vliet, L. J., and P. W. Verbeek, 1995, Estimators for orientation and anisotropy in digitized images: ASCI95, Proc. First Annual Conference of the Advanced School for Computing and Imaging (Heijen, NL, May 16-18), ASCI, 442–450.

Wu, X., and D. Hale, 2014, Horizon volumes with interpreted constraints: CWP Report XXX.